

# Towards Double Resonant Cavity Enhanced Second Harmonic Generation in Monolayer MoS<sub>2</sub>

Sai Shradha, Fatemeh Abtahi, Ziyang Gan, Heiko Knopf, Anna Fedotova, Franz J. F. Löchner, Antony George, Thomas Pertsch,\* Andrey Turchanin, and Falk Eilenberger

**A characteristic property of monolayered transition metal dichalcogenides is their strong nonlinear response. While they display a high conversion efficiency per atomic layer, due to their low thickness, the absolute value of their nonlinear response remains low. Here enhancement of the second harmonic generation (SHG) of monolayer MoS<sub>2</sub> through the design, fabrication, and characterization of a monolithic microcavity, which aims to be double resonant at a fundamental wavelength of  $\lambda = 800$  nm as well as its second harmonic, is demonstrated. The MoS<sub>2</sub> monolayers are embedded in such a cavity, with the aim to simultaneously enhance the light-matter interaction at the excitation wavelength and the SHG from the monolayers. A resonance enhancement for the SHG process is achieved through the cavity.**

## 1. Introduction

Among the many intriguing optical and optoelectronic properties of monolayer transition metal dichalcogenides (TMDs),<sup>[1–7]</sup> their strong second-order nonlinearity<sup>[8–14]</sup> stands out. This is because phase-matching conditions can be neglected due to the ultimate thinness of the monolayers that lack inversion symmetry. Broadband three-photon processes are particularly interesting in the context of ultrafast nonlinear light converters, such as optical parametric oscillators (OPOs) or optical parametric amplifiers (OPAs)<sup>[15]</sup> but also for broadband quantum light sources, which are based on the

spontaneous parametric down-conversion (SPDC) process. Indeed it has recently been shown, that thin but laterally extended SPDC sources are key for high-resolution quantum imaging schemes,<sup>[16]</sup> such as ghost imaging<sup>[17]</sup> or imaging with undetected photons.<sup>[18]</sup> The extremely low thickness of the materials, even though their nonlinear interaction strength per unit length is large, makes the overall conversion efficiency significantly low.

Hence, for the above-mentioned applications, a form of enhancement of the nonlinear interaction must be developed. Many studies have explored the use of plasmonic nanostructures,<sup>[19,20]</sup> photonic crystals,<sup>[21]</sup> and integration with metasurfaces and metamaterials<sup>[22,23]</sup> and microcavities<sup>[24–26]</sup> to enhance the various types of light emission from 2D TMDs. Cavities with a specific focus on enhancement the nonlinear properties of TMDs have also been investigated.<sup>[27–32]</sup> Bragg-type resonators stand out among these, not because of their high  $q$ -factor, but because of their simple mode structure and the availability of highly scalable and reproducible fabrication techniques. This may make them a suitable choice of applications and hence a worthwhile target for investigation. The microcavities we aim to design present the advantage of allowing for more than one resonance in the same system, and enhancing fundamental and second harmonic waves alike. Moreover, all possible applications would profit from monolithically embedded TMDs to mitigate their fragile nature and environmental sensitivity. For future applications, all processes should also be scalable and reproducible.

Here we demonstrate the integration of TMDs in a monolithic double-resonant cavity, composed of two distributed Bragg-reflectors (DBRs), which sandwich a dielectric spacer and a

S. Shradha, F. Abtahi, H. Knopf, A. Fedotova, F. J. F. Löchner, T. Pertsch, F. Eilenberger

Institute of Applied Physics  
Abbe Center of Photonics, Friedrich-Schiller-University  
Albert-Einstein-Straße 15, 07745 Jena, Germany  
E-mail: thomas.pertsch@uni-jena.de

S. Shradha  
Institute for Condensed Matter Physics  
Technical University of Darmstadt  
Hochschulstr. 6, 64289 Darmstadt, Germany

Z. Gan, A. George, A. Turchanin  
Institute of Physical Chemistry  
Friedrich Schiller University  
Lessingstraße 10, 07743 Jena, Germany

H. Knopf, T. Pertsch, F. Eilenberger  
Micro- and Nanostructured Optics  
Fraunhofer-Institute for Applied Optics and Precision Engineering (IOF)  
Albert-Einstein-Straße 7, 07745 Jena, Germany

H. Knopf, T. Pertsch, F. Eilenberger  
Max Planck School of Photonics  
Hans-Knöll-Straße 1, 07745 Jena, Germany

A. Fedotova  
Institute of Solid State Physics  
Friedrich-Schiller-University  
Helmholtzweg 3, 07743 Jena, Germany

 The ORCID identification number(s) for the author(s) of this article can be found under <https://doi.org/10.1002/adom.202300907>

© 2023 The Authors. Advanced Optical Materials published by Wiley-VCH GmbH. This is an open access article under the terms of the Creative Commons Attribution-NonCommercial License, which permits use, distribution and reproduction in any medium, provided the original work is properly cited and is not used for commercial purposes.

DOI: 10.1002/adom.202300907

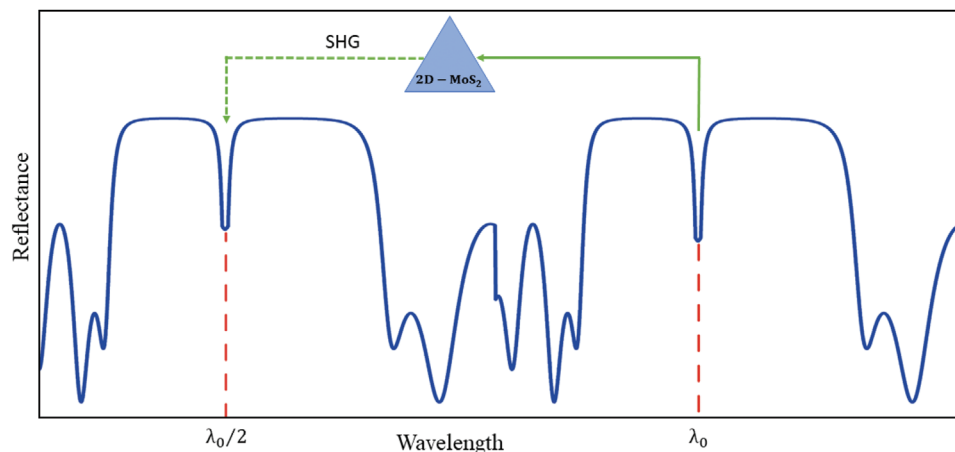


**Figure 1.** Schematic of the linear reflection spectra of the microcavity with resonances at  $\lambda_0$  and  $\lambda_0/2$ . The SHG from a single layer of  $\text{MoS}_2$  is depicted with  $\lambda_0$  as the excitation and achieving an SH intensity at wavelength  $\lambda_0/2$ .

monolayer of  $\text{MoS}_2$ . We characterize the system using linear and nonlinear optical spectroscopy. The spacer and DBRs are fabricated using a refined version of a previously reported physical vapor deposition technique,<sup>[33]</sup> which balances the requirements for the growth of high-grade dielectric materials with the sensitive nature of the monolayer crystals. The technique largely maintains the optical properties of the TMD crystals, without requiring an hBN-coating. The cavity is designed to exhibit resonances for the fundamental wave (FW) with a wavelength of  $\lambda_{\text{FW}} = 800$  nm and the second harmonic (SH) with a wavelength of  $\lambda_{\text{SH}} = 400$  nm. This design was chosen so as to enhance all modes which partake in the second harmonic generation (SHG) process, possibly yielding a dramatic increase of the conversion efficiency with less bandwidth penalty compared to the case where only SH or FW would be resonant.

## 2. Cavity Design

**Figure 1** shows a sketch of the linear reflection spectra of a doubly resonant cavity. It is designed with the fundamental resonance at a wavelength  $\lambda_{\text{FW}}$  and the secondary resonance at  $\lambda_{\text{SH}}$  thus enhancing the fundamental as well as SH response from the embedded monolayers.

The microcavity was designed with two DBRs with identical layer pairs.  $\text{SiO}_2$  and  $\text{TiO}_2$  were respectively chosen as the low and high refractive index materials. The TMD-crystal were embedded in a low-refractive index spacer layer composed of  $\text{SiO}_2$ . The top and bottom DBRs of the microcavity were made with 9 and 11 pairs of high and low refractive index layers, respectively. Each pair consisted of a layer of  $\text{SiO}_2$  with a design thickness of 179.8 nm and a layer of  $\text{TiO}_2$  with a thickness of 61.3 nm. These values of thicknesses were chosen so that their combined optical path length is  $\lambda_{\text{FW}}/2$ . The pairs are not composed of individual quarter-wave layers, instead, the optical path length difference of the  $\text{SiO}_2$  layer is chosen with a slightly larger path length of  $f \times \lambda_{\text{FW}}/4$  with  $f = 1.25$  and the thickness of  $\text{TiO}_2$  is thus reduced to  $(1 - f) \times \lambda_{\text{FW}}/4$ . Such a type of unbalanced layer pairing with  $f \neq 1$  incurs lower reflectivity for a given number of pairs but leads to the occurrence of a reflection band around  $\lambda_{\text{SH}}$ , which is a prereq-

uisite for a double resonance. In order to compensate for the shift due to dispersion an unbalanced layer pairing with  $f \neq 1$  is used. This incurs lower reflectivity for a given number of pairs but leads to the occurrence of a reflection band around  $\lambda_{\text{SH}}$ , which is a prerequisite for a double resonance. The characterization of the DBR can be found in Figure S5, Supporting Information. Both reflection bands can be clearly seen. In the simulations, the dispersion of the materials is taken into account; it leads to a blue shift of the reflection band at the second harmonic wavelength. The width of the spacer  $dS$  is then scanned over a set of possible values through simulations. Its modification induces a change in the wavelength of both resonances within the specific reflection bands defined by the respective mirrors. It is systematically changed until a pair of wavelengths with  $\lambda_{\text{FW}} = 2\lambda_{\text{SH}}$  is found. For our materials and geometries, this occurs for  $dS = 2.25 \lambda_{\text{FW}}/4$ . The simulation results are seen in Figure S1, Supporting Information.

## 3. Results and Discussion

**Figure 2a** shows a scanning electron microscope (SEM) image of the microcavity system. Here, the top and bottom DBRs, made from  $\text{SiO}_2$  and  $\text{TiO}_2$ , are separated by a spacer layer made of  $\text{SiO}_2$ , within which the TMD-crystal is embedded.

In order to determine the resonances of the microcavity, linear spectra of the system were measured using Perkin Elmer Lambda 950 system having a spot size of  $12 \times 4.5$  mm. Figure 2b,c show the results of multiple spectral measurements. In Figure 2b the reflection spectra from the cavity in the wavelength range  $300 \text{ nm} < \lambda < 1100 \text{ nm}$  is displayed. Two distinct reflection stopbands separated by the characteristic interference fringes of DBRs are observed. The first stopband, the one centered around  $\lambda_{\text{FW}}$ , is observed from roughly 720 to 930 nm (orange-shaded region). The narrower second harmonic reflection stopband ranges from  $\approx 400$  to 445 nm (green shaded region).

From this broadband spectra of the cavity, it can be seen that there appear resonance-like features, labeled F and S, at positions within the FH as well as SH reflection stopbands, respectively. To look more closely at these features, the spectra of the sample are remeasured with higher resolution in these

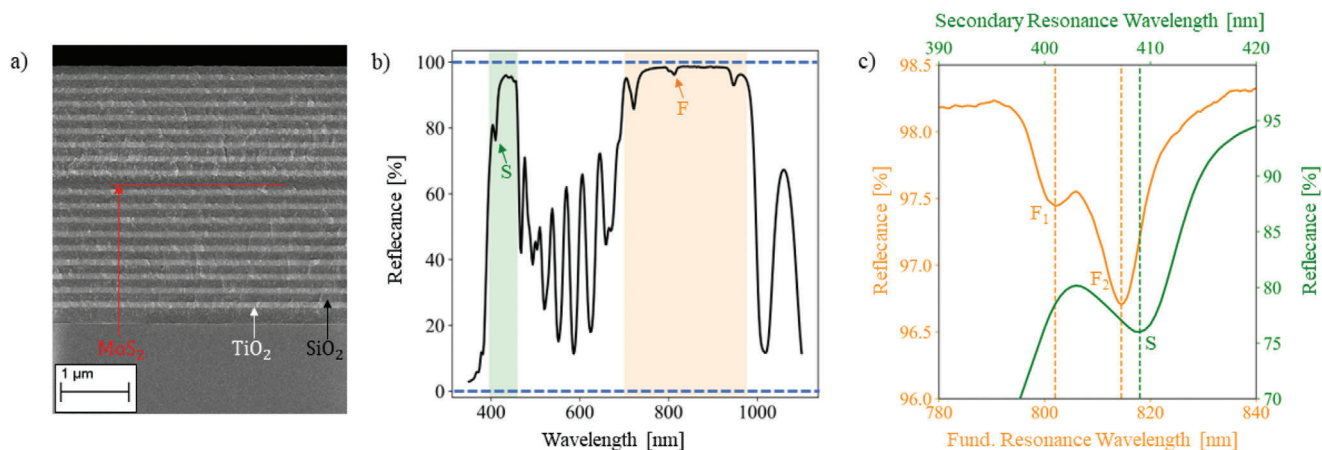


**Figure 2.** a) SEM cross-sectional image of a DBR cavity comprising of  $\text{SiO}_2$  as the low refractive index material and  $\text{TiO}_2$  as the high refractive index material. The position of the embedded monolayers is marked in red. b) Broad range linear spectra of the microcavity system with the fundamental resonance (F) in the first stopband (orange shaded region) and secondary resonance (S) in the second harmonic reflection stopband (green shaded region). c) Linear spectra in shorter ranges close to the fundamental (orange) and secondary (green) resonance. In the orange plot resonance like features are observed at 802 and 814.5 nm labeled as  $F_1$  and  $F_2$ , respectively. The secondary resonance, S, is observed at 409 nm.

respective ranges. Figure 2c shows the linear spectra of the cavity over narrower wavelength ranges. The orange colored plot shows the spectra in the vicinity of the fundamental resonance and the green plot is of that in the vicinity of the secondary resonance. In the orange plot, two discernible resonance features  $F_1$  and  $F_2$  are seen at 802 and 814.5 nm. The observation of two resonances is caused by the cavity being filled with monolayers in some regions while remaining empty in other regions. According to this argumentation, the  $F_1$  resonance corresponds to the parts of the cavity which are empty, and the  $F_2$  resonance to the parts of the cavity which are filled with monolayers. The overall shift to longer wavelengths (designed at 800 nm including the monolayer) is attributed to the formation of a slightly thicker spacer layer during fabrication than designed. Further optimization of the fabrication process could significantly reduce this offset.

In the green plot, a resonance S, indicated by the green dotted line is observed at 409 nm. It is likewise shifted to longer wavelengths (design at 400 nm) due to the thicker spacer layer. We do not observe a second resonance peak here, but it must be noted that the resonance is at the very edge of the stopband and any resonance at shorter wavelengths would be lost in the shoulder of the reflection roll-off at this edge. We thus conclude that the S resonance belongs to the filled cavity. We note that the S resonance does not perfectly coincide with  $F_2$ , which leads us to suggest that it cannot exploit the full double resonant SHG enhancement the microcavity was designed for. Nevertheless, both resonances overlap within their full width at half maximum, thus we still expect enhancement.

We thus proceed with the SHG experiment. **Figure 3a** shows the layout of the setup used to characterize the response from the monolayers.

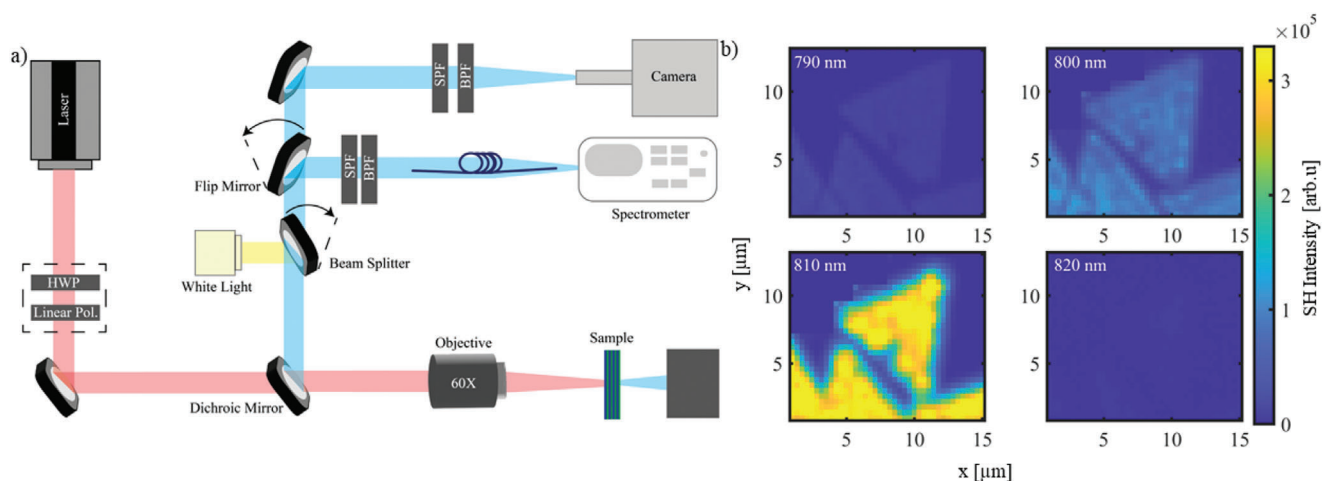


**Figure 3.** a) Optical spectroscopy setup for the characterization of the fundamental and SH response of the embedded monolayers. Two detection arms were used in order to acquire both intensity maps as well as spectral data. b) SH intensity maps of embedded  $\text{MoS}_2$  monolayers measured at excitation wavelengths of 790, 800, 810, and 820 nm.

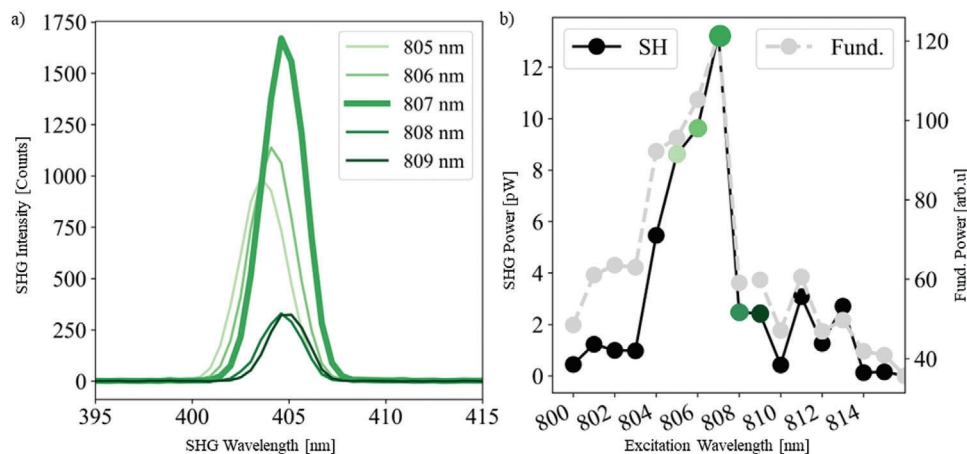


**Figure 4.** a) SHG spectra from the embedded monolayers measured with different excitation wavelengths. The broad line indicates the spectra for which the maximum SHG intensity was observed. b) SHG power (left axis, black curve) and fundamental power (right axis, grey dashed curve) as a function of the excitation wavelength. The green points correspond to the respective spectral measurements depicted in (a).

To observe the resonant behavior of the SHG from MoS<sub>2</sub> monolayers, SH intensity maps were obtained for different excitation wavelengths. These are presented in Figure 3b. With an excitation wavelength of 790 nm, the SHG intensity of the monolayers is negligible. When the excitation wavelength was increased to a value of 800 nm a discernible SHG intensity is visible from the triangular monolayer domains of MoS<sub>2</sub>. At 810 nm the SHG intensity from the monolayers increases further until finally showing no significant SHG at a pump wavelength of 820 nm. This variation of the SHG intensity from the MoS<sub>2</sub> monolayers as a function of the excitation wavelength is a clear indication of resonant behavior.

Following this observation, we carried out spectral measurements of the SHG intensity. In Figure 4a spectra for the SHG intensity for excitation wavelengths from 805 to 809 nm are displayed. It can be seen here that peak resonant SH efficiency is observed for an excitation wavelength of 807 nm. This spectrum is plotted bolder than the others for better visualization.

For a more systematic analysis of the dependence on the excitation wavelength, we plot the reflected fundamental power and SHG power as functions of the excitation wavelength while maintaining a constant incident power. The results can be seen in Figure 4b. To calculate the power of the SH intensity, we calibrated our measurement setup. The colored markers correspond to the spectra plotted in Figure 4a. With an excitation power of 2.5 mW at 807 nm, a peak SHG power of  $\approx 13$  pW is observed.

We clearly observe a resonant enhancement of the reflected FW as well as the amount of SH being generated. Both curves look rather similar with a peak at 807 nm and a generally similar shape. The FWHM was measured to be 2.5 and 5.2 nm for the SH and fundamental intensities, respectively. The resonance wavelength of 807 nm does not coincide with either of the measured resonances  $F_1$ ,  $F_2$ , or  $S$ . We hypothesize that this shift could be a consequence of humidity being adsorbed into the SiO<sub>2</sub>-layers between the various characterization stages.<sup>[34]</sup> This effect is well known for SiO<sub>2</sub> and is counteracted in commercial products, for example, by the application of a protective layer or by plasma treatment during fabrication, none of which was applied in our treatment. Nevertheless, we clearly observe resonant en-

hancement, which means that the overall validity of the approach is demonstrated.

In order to quantitatively evaluate the enhancement of the SHG from the embedded MoS<sub>2</sub>, we calculate the SHG conversion efficiency  $\eta$  from the observed SHG intensity. It is found that after the MoS<sub>2</sub> monolayers are transferred onto the bottom DBR, their SHG conversion efficiency  $\eta_{\text{pre}}$  is  $\approx 1.0 \times 10^{-11} \text{ W}^{-1}$ . Following their encapsulation by the top DBR the SHG conversion efficiency of the monolayers,  $\eta_{\text{post}}$  is  $\approx 1.6 \times 10^{-10} \text{ W}^{-1}$ . This indicates a factor of 16 enhancement in the SHG conversion efficiency of the monolayers at 807 nm excitation, due to the microcavity. While this is not a dramatic enhancement, we need to keep in mind that the laser bandwidth is larger than the cavity linewidth, which both prevents a large part of the laser power to reach the sample and also increases the pulse duration of the part that does reach the TMD. Given all the details we abstain from a comparison of the enhancement with the respective quality factors. Nevertheless, we would like to highlight that a significant enhancement by a factor of 16 was achieved through the application of the top mirror which closes the cavity, again underlining the validity of our approach.

#### 4. Conclusion

In this work, we have shown that TMD-monolayers can be embedded in a double-resonant monolithic DBR-cavity fabricated using an industry-scalable process. We show that the cavity can be designed in such a way that the two resonances correspond to a fundamental and second harmonic wavelength, although we observe slight deviations in fabricated samples. Such tolerancing issues could surely be overcome with more production runs. We show resonant second harmonic generation in such a sample, with peak SHG intensity occurring at a fundamental wavelength of 807 nm. The second harmonic resonance is accompanied by a resonance of the fundamental wave. We observe an overall on-resonance enhancement factor of 16 over the bare sample; however, we claim that this value could have been much higher if we had used a laser with a spectral bandwidth smaller than the resonance bandwidth. Our experiment demonstrates that we can

use DBR-cavity to enhance and tune the nonlinear interaction with 2D materials. This would be a highly interesting system for SPDC-based light sources for quantum imaging systems if pumped at the SH wavelength.

## 5. Experimental Section

**Cavity Fabrication:** For the fabrication of the microcavity system, ion-assisted physical vapor deposition process was used. The bottom DBR consisting of 11 layer pairs of SiO<sub>2</sub> and TiO<sub>2</sub> layers was deposited on a quartz substrate. After the transfer of the 2D materials, the top DBR which comprised of nine layer pairs was deposited. The deposition procedure was carried out using a background pressure of about 10<sup>-5</sup> mbar with a maximal process temperature of 80 °C.<sup>[33]</sup> This allowed for the growth of robust layers while ensuring the properties of the embedded monolayers were well maintained.

**Growth and Transfer of 2D-MoS<sub>2</sub>:** The 2D-TMD, in this case, MoS<sub>2</sub>, was first grown on a 300 nm SiO<sub>2</sub> layer on a Si substrate using the process of chemical vapor deposition.<sup>[35,36]</sup> Once the bottom DBR and the lower part of the spacer layer were deposited onto the substrate, the TMD monolayers were transferred onto it with a wet transfer technique<sup>[37,38]</sup> The remaining spacer layer and top DBR were then deposited on top of the monolayers, following the method discussed above.

**Preparation of Sample for SEM Imaging:** To obtain an SEM image of the cross-section of the microcavity, one of the edges of the sample was cleaved using a diamond cutter. This exposed the layer stacks that were subsequently imaged with the SEM.

**Linear Characterization:** The characterization of the linear reflection from the microcavity was carried out using a Perkin Elmer Lambda 950 spectrometer which used a deuterium light source in the UV range and a tungsten halogen source in the NIR range.

**SHG Measurements:** For the characterization of the SHG from the embedded monolayers, a femtosecond Ti:Sa pulsed laser with a pulsewidth of 140 fs, a repetition rate of 80 MHz, and FWHM of 6.5 nm for an excitation of 800 nm was used. The power of the laser beam was maintained at 2.5 mW using a half wave plate (HWP). The HWP was followed by a linear polarizer that ensured the excitation had a fixed linear polarization (vertically polarized) state. The laser beam was focused using a 60x objective onto the cavity. The reflected FW and SH maps were obtained by scanning the sample at the laser focus. In order to ensure selective reflection of the SHG, a custom-made dichroic mirror was used. For measurements of the SH intensity, a combination of a 600 nm short pass filter and band pass filter with a transmission range of 350–610 nm was incorporated into the detection arm. Figure 3a shows the setup used.

## Supporting Information

Supporting Information is available from the Wiley Online Library or from the author.

## Acknowledgements

The authors acknowledge the financial support of the Deutsche Forschungsgemeinschaft (DFG) through CRC 1375 NOA (Project B2 and B3), SPP2244 (Project TU149/13-1) DFG grant TU149/16-1. The authors gratefully acknowledge the financial support by the German Federal Ministry of Education and Research via “2D Nanomaterialien für die Nanoskopie der Zukunft,” FKZ no. 13XP5053A and the European Union, the European Social Funds and the Federal State of Thuringia under grant ID no. 2021FG1004.

Open access funding enabled and organized by Projekt DEAL.

## Conflict of Interest

The authors declare no conflict of interest.

## Data Availability Statement

The data that support the findings of this study are available from the corresponding author upon reasonable request.

## Keywords

microcavity, second harmonic generation, transition metal dichalcogenides

Received: April 17, 2023

Revised: July 18, 2023

Published online: August 18, 2023

- [1] K. F. Mak, C. Lee, J. Hone, J. Shan, T. F. Heinz, *Phys. Rev. Lett.* **2010**, *105*, 136805.
- [2] A. Splendiani, L. Sun, Y. Zhang, T. Li, J. Kim, C.-Y. Chim, G. Galli, F. Wang, *Nano Lett.* **2010**, *10*, 1271.
- [3] B. Radisavljevic, A. Radenovic, J. Brivio, V. Giacometti, A. Kis, *Nat. Nanotechnol.* **2011**, *6*, 147.
- [4] Q. H. Wang, K. Kalantar-Zadeh, A. Kis, J. N. Coleman, M. S. Strano, *Nat. Nanotechnol.* **2012**, *7*, 699.
- [5] H. R. Gutiérrez, N. Perea-López, A. L. Elías, A. Berkdemir, B. Wang, R. Lv, F. López-Urías, V. H. Crespi, H. Terrones, M. Terrones, *Nano Lett.* **2013**, *13*, 3447.
- [6] F. Xia, H. Wang, D. Xiao, M. Dubey, A. Ramasubramaniam, *Nat. Photonics* **2014**, *8*, 899.
- [7] K. F. Mak, J. Shan, *Nat. Photonics* **2016**, *10*, 216.
- [8] L. M. Malard, T. V. Alencar, A. P. M. Barboza, K. F. Mak, A. M. de Paula, *Phys. Rev. B* **2013**, *87*, 201401.
- [9] N. Kumar, S. Najmaei, Q. Cui, F. Ceballos, P. M. Ajayan, J. Lou, H. Zhao, *Phys. Rev. B* **2013**, *87*, 161403.
- [10] C. Janisch, Y. Wang, D. Ma, N. Mehta, A. L. Elías, N. Perea-López, M. Terrones, V. Crespi, Z. Liu, *Sci. Rep.* **2014**, *4*, 5530.
- [11] G. Wang, X. Marie, I. Gerber, T. Amand, D. Lagarde, L. Bouet, M. Vidal, A. Balocchi, B. Urbaszek, *Phys. Rev. Lett.* **2015**, *114*, 097403.
- [12] M. L. Trolle, Y.-C. Tsao, K. Pedersen, T. G. Pedersen, *Phys. Rev. B* **2015**, *92*, 161409.
- [13] J. Zhang, W. Zhao, P. Yu, G. Yang, Z. Liu, *2D Mater.* **2020**, *7*, 042002.
- [14] K. Ullah, Y. Meng, Y. Shi, F. Wang, *Adv. Opt. Mater.* **2022**, *10*, 2101860.
- [15] C. Trovatiello, A. Marini, X. Xu, C. Lee, F. Liu, N. Curreli, C. Manzoni, S. D. Conte, K. Yao, A. Ciattoni, J. Hone, X. Zhu, P. J. Schuck, G. Cerullo, *Nat. Photonics* **2021**, *15*, 6.
- [16] O. S. Magaña-Loaiza, R. W. Boyd, *Rep. Prog. Phys.* **2019**, *82*, 124401.
- [17] P.-A. Moreau, E. Toninelli, T. Gregory, M. J. Padgett, *Laser Photonics Rev.* **2018**, *12*, 1700143.
- [18] G. B. Lemos, V. Borish, G. D. Cole, S. Ramelow, R. Lapkiewicz, A. Zeilinger, *Nature* **2014**, *512*, 409.
- [19] B. Lee, J. Park, G. H. Han, H.-S. Ee, C. H. Naylor, W. Liu, A. C. Johnson, R. Agarwal, *Nano Lett.* **2015**, *15*, 3646.
- [20] X.-X. Wu, W.-Y. Jiang, X.-F. Wang, L.-Y. Zhao, J. Shi, S. Zhang, X. Sui, Z.-X. Chen, W.-N. Du, J.-W. Shi, Q. Liu, Q. Zhang, Y. Zhang, X.-F. Liu, *ACS Nano* **2021**, *15*, 1291.
- [21] X. Ge, M. Minkov, S. Fan, X. Li, W. Zhou, *npj 2D Mater. Appl.* **2019**, *3*, 16.
- [22] P. K. Jha, N. Shitrit, X. Ren, Y. Wang, X. Zhang, *Phys. Rev. Lett.* **2018**, *121*, 116102.
- [23] F. Spreyer, R. Zhao, L. Huang, T. Zentgraf, *Nanophotonics* **2020**, *9*, 351.
- [24] X. Liu, T. Galfsky, Z. Sun, F. Xia, E. chen Lin, Y.-H. Lee, S. Kéna-Cohen, V. M. Menon, *Nat. Photonics* **2015**, *9*, 30.

- [25] X. Liu, W. Bao, Q. Li, C. Ropp, Y. Wang, X. Zhang, *Phys. Rev. Lett.* **2017**, 119, 027403.
- [26] X. Huang, X. Feng, L. Chen, L. Wang, W. C. Tan, L. Huang, K.-W. Ang, *Nano Energy* **2019**, 62, 667.
- [27] J. K. Day, M.-H. Chung, Y.-H. Lee, V. M. Menon, *Opt. Mater. Express* **2016**, 6, 2360.
- [28] F. Yi, M. Ren, J. C. Reed, H. Zhu, J. Hou, C. H. Naylor, A. T. C. Johnson, R. Agarwal, E. Cubukcu, *Nano Lett.* **2016**, 16, 1631.
- [29] T. K. Fryett, K. L. Seyler, J. Zheng, C.-H. Liu, X. Xu, A. Majumdar, *2D Mater.* **2016**, 4, 015031.
- [30] J. Shi, X. Wu, K. Wu, S. Zhang, X. Sui, W. Du, S. Yue, Y. Liang, C. Jiang, Z. Wang, W. Wang, L. Liu, B. Wu, Q. Zhang, Y. Huang, C.-W. Qiu, X. Liu, *ACS Nano* **2022**, 16, 13933.
- [31] R. Zhou, A. Krasnok, N. Hussain, S. Yang, K. Ullah, *Nanophotonics* **2022**, 11, 3007.
- [32] H. Chen, Y. Tang, T. Jiang, G. Li, in *Comprehensive Nanoscience and Nanotechnology*, 2nd ed., (Eds: D. L. Andrews, R. H. Lipson, T. Nann), Vol. 1, Academic Press, Oxford **2019**, pp. 305–318.
- [33] H. Knopf, N. Lundt, T. Bucher, S. Höfling, S. Tongay, T. Taniguchi, K. Watanabe, I. Staude, U. Schulz, C. Schneider, F. Eilenberger, *Opt. Mater. Express* **2019**, 9, 598.
- [34] H. Ehlers, T. Groß, M. Lappschies, D. Ristau, *Vak. Forsch. Prax.* **2004**, 16, 284.
- [35] A. George, C. Neumann, D. Kaiser, R. Mupparapu, T. Lehnert, U. Hübner, Z. Tang, A. Winter, U. Kaiser, I. Staude, A. Turchanin, *J. Phys. Mater.* **2019**, 2, 016001.
- [36] S. Shree, A. George, T. Lehnert, C. Neumann, M. Benelajla, C. Robert, X. Marie, K. Watanabe, T. Taniguchi, U. Kaiser, B. Urbaszek, A. Turchanin, *2D Mater.* **2019**, 7, 015011.
- [37] E. Najafidehaghani, Z. Gan, A. George, T. Lehnert, G. Q. Ngo, C. Neumann, T. Bucher, I. Staude, D. Kaiser, T. Vogl, U. Hübner, U. Kaiser, F. Eilenberger, A. Turchanin, *Adv. Funct. Mater.* **2021**, 31, 2101086.
- [38] A. Winter, A. George, C. Neumann, Z. Tang, M. J. Mohn, J. Biskupek, N. Masurkar, A. L. M. Reddy, T. Weimann, U. Hübner, U. Kaiser, A. Turchanin, *Carbon* **2018**, 128, 106.